Excited states of defect linear arrays in silicon: A first-principles study based on hydrogen cluster analogs

W. Wu,* P. T. Greenland, and A. J. Fisher
UCL Department of Physics and Astronomy and London Centre for Nanotechnology, University College London, Gower Street, London WC1E 6BT, United Kingdom

Nguyen H. Le, S. Chick, and B. N. Murdin
Advanced Technology Institute and Department of Physics, University of Surrey, Guildford GU2 7XH, United Kingdom

(Received 27 October 2017; published 29 January 2018)

Excited states of a single donor in bulk silicon have previously been studied extensively based on effective mass theory. However, proper theoretical descriptions of the excited states of a donor cluster are still scarce. Here we study the excitations of lines of defects within a single-valley spherical band approximation, thus mapping the problem to a scaled hydrogen atom array. A series of detailed time-dependent Hartree-Fock, time-dependent hybrid density-functional theory and full configuration-interaction calculations have been performed to understand linear clusters of up to 10 donors. Our studies illustrate the generic features of their excited states, addressing the competition between formation of interdonor ionic states and intradonor atomic excited states. At short interdonor distances, excited states of donor molecules are dominant, at intermediate distances ionic states play an important role, and at long distances the intradonor excitations are predominant as expected. The calculations presented here emphasize the importance of correlations between donor electrons, and are thus complementary to other recent approaches that include effective mass anisotropy and multivalley effects. The exchange splittings between relevant excited states have also been estimated for a donor pair and for three-donor arrays; the splittings are much larger than those in the ground state in the range of donor separations between 10 and 20 nm. This establishes a solid theoretical basis for the use of excited-state exchange interactions for controllable quantum gate operations in silicon.

DOI: 10.1103/PhysRevB.97.035205

I. INTRODUCTION

After decades of development and incorporation of many new materials, the core material technology of microelectronics remains based on silicon. Impurities in silicon play a vital role in its transport, magnetic, and optical properties [1]. The recent encouraging progress in deterministic positioning of dopants in silicon [2–4] promises atom-by-atom design and bottom-up fabrication of silicon-based nanodevices; such nanostructures can offer not only an ultimate limit for conventional electronic components such as wires [5] and tunnel structures [6], but also a potential platform for many applications in silicon quantum electronics [1], and ultimately for new technologies that exploit the quantum properties of electron spin and orbital motion [7–12]. An obvious candidate for a quantum bit (qubit) is a donor electron spin: the spin-lattice relaxation time (T_1) of donor electron spins in silicon has been measured to be up to a few thousand seconds [13,14], and the coherence time (T_2) is up to milliseconds, limited only by interactions with neighboring electron or nuclear spins. The T_2 can be enhanced further, to several seconds by the use of field-insensitive "clock transitions" [15], and even further by the use of isotopically pure ^{28}Si.

Recent progress has shown that the orbital degree of freedom of a dopant electron in silicon can also be controlled and could potentially itself serve as a qubit. Terahertz (THz) optical excitations (tuned to an energy-level spacing of approximately meV) can be used to manipulate and detect Rydberg states of donors by using a free-electron laser [16–19]. In the density range where donor pairs are dominant, the optical field has been used to detect and control the electron tunneling between donor pairs of phosphorus and antimony [20], while in three-donor clusters, the optical excitation (de-excitation) of a shallower "control" donor has the potential to switch on (off) the exchange interaction between the other two deeper donors, thus forming an optically controlled quantum gate [21,22]. There has also been growing experimental interest in performing quantum simulations [9,23] in donor clusters. Arrays of dopants in silicon [9] and quantum dots [23] have been fabricated for the quantum simulation of the Fermi-Hubbard model; the freedom to position the atoms arbitrarily enables tuning of correlations by varying the interdonor distance [24]. Such a platform could be enhanced by the ability to probe the state of the electrons using optical absorption. It is therefore timely to study theoretically the optical properties of multiatom donor clusters such as arrays, and in particular the effect of excitation on the spin-spin interaction.

The electronic structure of a single dopant in silicon (or germanium) has been extensively studied previously [25–28]. There are mainly two types of methodologies, including

*wei.wu@ucl.ac.uk

 ©2018 American Physical Society

effective mass theory (EMT) and atomistic tight-binding (ATB) methods. Within EMT, either anisotropic hydrogenic trial wave functions [26] or a Coulomb potential deformed through a coordinate transformation [27] have been used to account for the anisotropy of the conduction-band minimum. These calculations were refined in the 1970s by adding multivalley effect (MVE) and the effects of deviations from a pure Coulomb potential [29], producing agreement with experimental spectra. Recently, Gamble *et al.* solved the Shindo-Nara multivalley equation [30] by including the full Bloch wave functions of silicon [31], showing a good agreement with the experimental energy spectrum of single phosphorus atoms, and also gave theoretical values for donor-donor tunnel couplings. The ATB calculation is another commonly used method, which considers the full lattice structure of the host material [32,33]. Both approaches have produced theoretical results in excellent agreement with the experimental ground-state energy spectrum and hyperfine Stark shift of single phosphorus donors in silicon. For two electrons in a single donor (D^-), ATB calculations followed by a self-consistent Hartree method were used to account for the electron-electron interaction in a mean-field way, while neglecting exchange [34,35]. A full configuration-interaction (FCI) computation has been performed for D^- with single-electron wave functions obtained from the atomistic tight-binding method [36,37].

Studies of impurity clusters in silicon have gained a significant surge recently [38–40]. The exchange interactions between donors have been studied within EMT, combined with the Heitler-London formalism [41], including variable binding energies [42]. The electronic structure of a donor pair has been studied by using CI within the 1s manifold [39]. Larger donor clusters have been studied by using density-functional theory (DFT) and the GW method (for bulk silicon) combined with EMT [40]; this approach included implicitly the electron correlations in the bulk, but missed the explicit Coulomb interaction between electrons within the multidonor "molecule." A combination of EMT and ATB has been employed to calculate the electronic structure of thin dopant chains and to study the localization of donor electrons owing to disorder [38]. In the calculations to date, the electron correlations are either at least partly absent, or confined to the lowest manifold of the 1s ground states of single donors and donor pairs.

The multivalley effect and central-cell corrections (CCC) are important for the 1s ground states where the electron is close to the defect core, but not so important for the more diffuse excited states. On the other hand, in the description of the electronic structure of donor clusters, the electron-electron correlations are known to play a vital role in both optical and transport properties [43]. For example, the optical absorption shows a strong signature of the ionic state of a donor pair (D^+-D^- state, also called a charge-transfer state in Ref. [43]), in which an electron hops from one donor to the other, leaving a hole behind. The ionic state here is effectively a bound state of the holons and doublons that are used to analyze excitations of the Hubbard model in solid-state physics [44,45]. However, such low-energy ionic states appear only if proper account is taken of the intracluster correlations. In addition, the spherical-band approximation (replacing the anisotropic effective mass by using a single average one) turned out to be good in predicting the ground-state energy of donors in silicon [29]. Taken together, these facts suggest that a combination of an isotropic Hamiltonian, and wave function within the spherical band approximation [29], with highly accurate first-principles methods to treat electron correlation is a suitable starting point to describe the excited states of donor clusters.

Here, we report a systematic study of the orbital excited states and related exchange splittings of donor arrays in silicon, within the isotropic approximation to effective-mass theory but retaining a full treatment of correlations among the donor electrons. In our calculations, we use hydrogen atoms to represent silicon donors, then compute the excited states by using CI, time-dependent Hartree-Fock (TDHF) [46,47], and time-dependent density-functional theory (TDDFT), and at the end scale the excitation energies by using the effective mass and dielectric constant of silicon. From these calculations, we are able to obtain a rich spectrum of physics for the excited states. We have performed FCI calculations for linear arrays consisting of up to three donors, in which the electron correlations are fully taken into account, which we used to benchmark the exchange-correlation functional in TDDFT. Our TDDFT calculations provide a good approximation to the CI results for these small arrays, and then are extended to describe the excited states of arrays consisting of up to 10 donors. From the perspective of molecular physics, the electronic structure of H_2 is very well known, but the solid-state environment fixes the donor separations at implantation; hence these calculations emphasize molecular excited states in unstable hydrogen clusters far from equilibrium.

The rest of the paper is organized as follows: we introduce the computational details in Sec. II, discuss TDHF, TDDFT, and FCI results in Sec. III, and draw some general conclusions in Sec. IV.

II. COMPUTATIONAL DETAILS

We work in the single-valley isotropic approximation to effective mass theory, in which a shallow donor is a direct analog of a hydrogen atom. We therefore neglect (i) the anisotropy of the conduction band, (ii) deviations of the potential from Coulomb form (in particular "central-cell" corrections), and (iii) any resulting intervalley coupling. However, we include a careful treatment of the correlations between the bound electrons.

A. Effective-mass theory

Within the single-valley approximation, the effective-mass equation [25,26] reads

$$\left[\epsilon_n\left(\vec{k}_0+\frac{1}{i}\nabla\right)+U\right]F_n=\epsilon F_n, \tag{1}$$

where the band energy ϵ_n is expanded around the band extremum $\vec{k}_0$ to second-order terms in $(1/i)\nabla$. F_n is the envelope function, in terms of which the donor wave function is expanded using

$$\psi=\sum_n \alpha_n F_n(\vec{r})\phi_{n\vec{k}_0}(\vec{r}), \tag{2}$$

where $\phi_{n\vec{k}_0}(\vec{r})=e^{i\vec{k}\cdot\vec{r}}u_{n\vec{k}_0}(\vec{r})$ is a Bloch function at the band extremum.

In the isotropic approximation, the effective mass tensor is replaced by a single averaged effective mass m^*, resulting in an effective isotropic equation for the envelope function, which is then independent of the index n:

$$\left(-\frac{\hbar^2}{2m^*}\nabla^2 - \frac{e^2}{4\pi\epsilon_0\epsilon_r r} - \epsilon\right)F(\vec{r}) = 0, \tag{3}$$

where ϵ_r is the relative permittivity of the host. In this paper, we will work with this isotropic equation as our starting point. For silicon, $m^* = 0.33m_e$ and $\epsilon_r = 11.7$; this leads to a set of scaled atomic units for the hydrogenic impurity problem (length $a_0^* = 1.94$ nm, energy $\mathrm{Ha}^* = 62$ meV). For multi-donor systems, the screened Coulomb interaction between electrons $\frac{e^2}{4\pi\epsilon_0\epsilon_r|\vec{r}_1-\vec{r}_2|}$ can be scaled as well. Thus we have a Hamiltonian in units of a_0^* and the effective Hartree (Ha^*) that reads

$$\hat{H} = \sum_{i,A}\left(-\frac{1}{2}\nabla_i^2 - \frac{1}{|\vec{r}_i - \vec{R}_A|}\right) + \sum_{i<j}\frac{1}{|\vec{r}_i - \vec{r}_j|}, \tag{4}$$

where A runs over all the donor sites (i and j label electrons). To solve this equation, standard molecular *ab initio* computational methods, including CI, TDHF, and TDDFT, can be used to compute excited states.

B. First-principles calculation methods

For the CI calculations, we used a specially constructed basis set designed to reproduce within an accuracy of 10^{-5} Ha^* the excitation energies of $2s$, $2p_x$, $2p_y$, and $2p_z$ states of a hydrogen atom. By extending the aug-cc-pCV5Z basis set for hydrogen [48], we found that 12 (11) Gaussians with almost equally tempered exponents ranging from $402.0/a_0^{*2}(1.1/a_0^{*2})$ to $0.005/a_0^{*2}(0.000976563/a_0^{*2})$ are required for s (p) symmetries, giving a total basis set of 45 Gaussians per atom, as shown in Table I. This basis set was then employed consistently throughout all the CI calculations. CI calculations were performed for a donor pair (DA2) and a uniform three-donor array (DA3) using the GAUSSIAN 09 [49,50] and MOLPRO [51–54] codes. We used the symmetry-adapted cluster/configuration interaction (SAC-CI) method [50], as implemented in GAUSSIAN 09, to calculate the energies and oscillator strengths. We also performed FCI calculations in MOLPRO [53,54], which gives only the excitation energies: the computation of oscillator strengths within FCI has not been implemented in MOLPRO, so they were instead estimated using the GAUSSIAN 09 code. The SAC-CI methods implemented in GAUSSIAN 09 can be used to compute the total-spin eigenstates, whereas MOLPRO produces eigenstates of a given spin projection. FCI calculations can produce accurate excitation energies and yield FCI wave functions. However, the FCI procedure is limited by the size (the number of electrons and the number of basis functions) of the system as the number of configurations taken into account increases factorially. We have performed the CI calculations for DA2 and DA3 with increments of $\approx 0.07a_0^*$ ($\approx$0.14nm, approximately one quarter of silicon lattice constant).

As an alternative to CI, TDDFT has been widely used to compute approximately the excited states of molecules and solids [55,56], while including an approximate treatment of electronic correlations (detailed reviews can be found in Ref. [57]). In TDDFT, the computed excitation energies correspond to the poles of the linear response of the charge density to an external time-dependent stimulus. The linear response of charge densities of the real system is calculated by using the response in a noninteracting reference system, via a formalism similar to the Dyson equation. For our TDDFT calculations, we use an adiabatic hybrid-exchange functional [58–60] with the proportion of exact Fock exchange tuned to match the analytical excitation energies of $2s$, $2p_x$, $2p_y$, and $2p_z$ states of a hydrogen atom as accurately as possible; this can be thought of as seeking the best (approximate) cancellation of the self-interaction error in the isolated atom. The optimal proportion of exact Fock exchange was found to be 40% in order to match the $1s \rightarrow 2sp$ excitation energies of a hydrogen atom (up to 10^{-2} Ha^*), in comparison with 20% in the conventional hybrid-exchange functional B3LYP [61]. We have also tuned the basis set to reproduce the $1s \rightarrow 2sp$ excitation energies, and found that the range for the Gaussian exponents is between $402.0/a_0^{*2}$ $(1.1/a_0^{*2})$ to $0.000625/a_0^{*2}$ $(0.00390625/a_0^{*2})$ for the s (p) symmetry, leading to 43 Gaussian functions, as shown in Table I. The basis set and corresponding fine-tuned exchange-correlation functional, implemented in GAUSSIAN 09 code, were then used in all the TDDFT calculations for the excited states of DA2, all the way up to DA10 (uniform ten-donor array).

TABLE I. Gaussian basis set to perform TDDFT calculations, which is slightly more diffuse than FCI calculations. Here, BF=basis function, Exp.=exponential, and Cont.=contraction.

	TDHF and FCI		TDDFT		
Shell	BF	Exp.	Cont.	Exp.	Cont.
S	1	402.0	0.05088	402.0	0.05088
		60.24	0.03948	60.24	0.03948
		13.73	0.20427	13.73	0.20427
		3.905	0.81844	3.905	0.81844
	2	1.283	1.0	1.283	1.0
	3	0.6	1.0	0.6	1.0
	4	0.3	1.0	0.3	1.0
	5	0.15	1.0	0.15	1.0
	7	0.07279	1.0	0.07279	1.0
	8	0.0207	1.0	0.0207	1.0
	9	0.01	1.0	0.01	1.0
	10	0.005	1.0	0.005	1.0
	11			0.0025	1.0
	12			0.00125	1.0
	13			0.000625	1.0
P	1	1.1	1.0	1.1	1.0
	2	0.5	1.0	0.5	1.0
	3	0.25	1.0	0.25	1.0
	4	0.125	1.0	0.125	1.0
	5	0.0625	1.0	0.0625	1.0
	6	0.03125	1.0	0.03125	1.0
	7	0.015625	1.0	0.015625	1.0
	8	0.0078125	1.0	0.0078125	1.0
	9	0.00390625	1.0	0.00390625	1.0
	10	0.00195313	1.0		
	11	0.000976563	1.0		

A third option for the solution of the many-electron excited-state problem is TDHF, which can be regarded as including exchange but no correlations. TDHF methods can be thought of as including some doubly-excited configurations, and eliminate the self-interaction error, which cannot in practice be removed completely in TDDFT [62]. We have performed TDHF calculations [47], implemented in the GAUSSIAN 09 code [49] and using the same basis set as the FCI calculations for up to ten-donor arrays. TDHF and TDDFT methods share similar formalisms to compute the excitation energies although they use different ground states as the starting point, and the exchange-correlation functional in TDDFT is replaced by exchange integrals in TDHF. We use the TDHF calculations to provide an uncorrelated reference calculation to compare with FCI and TDDFT.

We found that in order to represent properly the states at large donor separations, it is important to allow the static DFT and HF solutions to find ground states with broken-symmetry form [63], in which the Kohn-Sham (or HF) states of opposite spin components are free to localize on different donors. Although such a solution breaks both the spatial and spin symmetries of the complex, it allows the best approximate representation of the antiferromagnetic correlations in the ground state within a single Slater determinant [63]. In practice, we find such broken-symmetry configurations are favored when the atomic separation is greater than approximately 5 $a_0^* \approx$ 10 nm (this can be compared with the experimentally observed Mott transition in three-dimensional doped silicon, where the electrons localize below a density of 3.7×10^{18} cm^{-3}, corresponding to a mean separation of approximately 6.5 nm) [43]. As a result, our TDDFT and TDHF calculations conserve the total spin projection M_S on the quantization axis, but not the total spin quantum number S. For TDDFT and TDHF calculations, we have selected reasonable number of excited-state energy eigenvalues to keep the image clear.

The arrays formed by the uniformly spaced donors are arranged along the z direction throughout the paper, and we discuss all symmetries within the $D_{\infty h}$ point group. We use distance units of nm and energy units of meV throughout. For all the plots of the oscillator strengths, the excitation energies are computed as the energy differences between excited states and the ground state with the same spin, while for the plots of excitation energies, all states are referred to the overall lowest-spin ground state.

III. RESULTS

A. Two and three donors: configuration interaction calculations

1. Two donors

The ground state of a donor pair has a symmetry of $^1\Sigma_g^+$. In Fig. 1, we plot the energies of low-lying excited states, with different spatial and spin symmetries ($^{1,3}\Sigma_{u,g}^+$ and $^{1,3}\Pi_{u,g}^+$), as a function of donor separation (singlet in solid curves and triplet in dashed). These excited states converge to the excitations of the s and p states either in the $n = 2$ or 3 shells in the limit of isolated donors. The nature of the states is familiar from the previous experimental and theoretical studies of a H_2 molecule [64,65]. The four lowest excitation energies of $^1\Sigma_u^+$, $^1\Sigma_g^+$, and $^1\Pi_{u,g}^+$ symmetries are shown in Figs. 1(a)–1(c), respectively (in each case two states dissociate to $n = 2$ and another two to $n = 3$ shells). The singlet excitation energies all rise to ≈40 meV at small separations, where the two donors are strongly coupled, forming a molecular complex. The dominant optical transitions are then between these delocalized molecular orbitals.

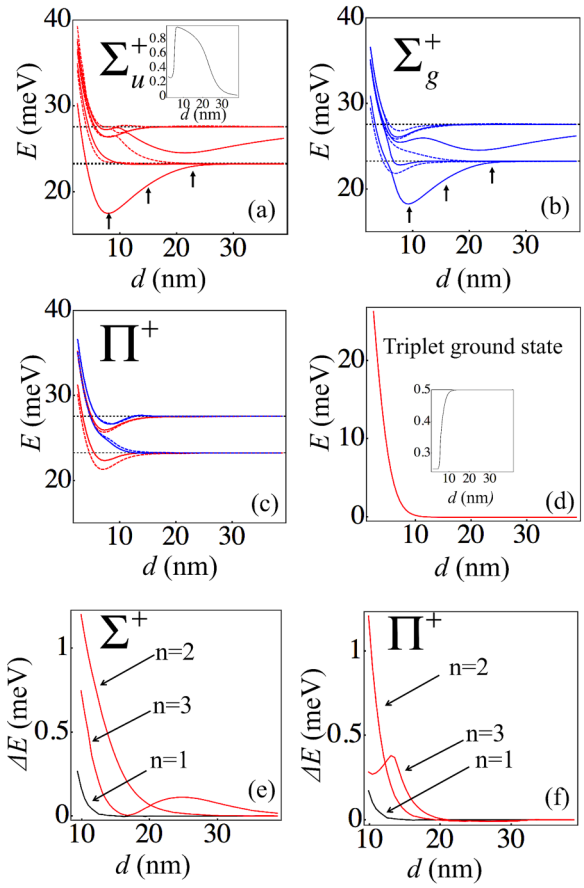

FIG. 1. The excitation energies of DA2 as a function of donor separation, calculated using FCI methods. The first three panels show excitation energies of different spatial symmetries for states converging to $n = 2$ and $n = 3$ transitions, relative to the overall singlet ground state ($^1\Sigma_g^+$): (a) $^1\Sigma_u^+$ and $^3\Sigma_u^+$, (b) $^1\Sigma_g^+$ and $^3\Sigma_g^+$ and (c) $^1\Pi_{u,g}^+$ and $^3\Pi_{u,g}^+$. Singlet states are indicated by solid lines, triplets by dashed lines. Odd-parity (u) excitations are shown in red, even-parity (g) excitations in blue (online)—hence the red (blue) states are accessible by electric-dipole-allowed transitions from the even-parity singlet (odd-parity triplet) ground states. The inset to (a) shows the CI coefficient of the ionic state in the total wave function of the lowest $^1\Sigma_u^+$ excitation as a function of donor separation. The splitting between the $^1\Sigma_g^+$ singlet and $^3\Sigma_u^+$ triplet ground states within the lowest ($1s$) manifold as a function of donor separation is shown in (d); the inset is the probability of the double excitation to the $1s$ antibonding state in the CI total ground-state wave function, as a function of donor separation. The exchange splittings between corresponding optically accessible excited spin states are shown in (e) and (f): $^1\Sigma_u^+$ and $^3\Sigma_g^+$ excited states (corresponding to excitation from the lowest manifold with z-, in red for both $n = 2$ and $n = 3$ states) are shown in (e), $^1\Pi_u^+$ and $^3\Pi_g^+$ states (x, y polarization, in red) in (f), along with the ground-state exchange splittings (in black).

At various points, the lowest $^1\Sigma_u^+$ and $^1\Sigma_g^+$ states are formed by different combinations of $1s$, $2s$, and $2p_z$ atomic orbitals

[43,65]: the different regimes are illustrated by the arrows in Figs. 1(a) and 1(b). At small separations (the leftmost arrow marking the minimum excitation energy of ≈17 meV, $d <$ 7 nm) the excitations are predominantly between molecular orbitals, converging to the single-electron $2p\sigma$ ($^1\Sigma_u^+$) and $2s\sigma$ ($^1\Sigma_g^+$) excitations in the united-atom limit [64]. Near the center arrows (7 nm $\leqslant d \leqslant$ 22 nm), these lowest singlet excitations correspond closely to the ionic (or charge-transfer) excited state, which can also be thought of as arising from the transition between the $1s\sigma$ (bonding) and $1s\sigma^*$ (antibonding) states. The excitation energy has a minimum of ≈17 meV at an interdonor distance of ≈7 nm. At $d \approx 22$ nm (centre arrow), there is a transition where the ionic state anticrosses with the $1s \rightarrow 2sp$ transition; at larger separations the lowest excitation has a predominantly single-atom $1s \rightarrow 2sp$ character, while the charge-transfer transition increases further in energy towards the $1s \rightarrow 3sp$ excited states (rightmost arrow). Meanwhile, four further $1s \rightarrow 2sp$ transitions ($^1\Sigma_{u,g}^+$ and $^1\Pi_{u,g}^+$) persist with their energies almost unaffected as long as the donor separation is larger than ≈12 nm, below which the hybridization between orbitals in the $n = 2$ shell on different atoms starts to become significant. The $^1\Sigma_g^+$ state becomes the $3s\sigma$ state of the united atom, the $^1\Sigma_u^+$ state leads to the united-atom $3p\sigma$ excitation, while the $^1\Pi_u^+$ drops briefly in energy to form the $2p\pi$ excitation and the $^1\Pi_g^+$ rises steeply to form the $3d\pi$ excitation. The upper band of $^1\Sigma_{u,g}^+$ charge-transfer states (beyond the anticrossing with the single-atom $n = 2$ transition) transforms below 22 nm (rightmost arrow) into a combination of $2s$, $2p_z$, $3s$ and $3p_z$ atomic excitations, which rises gradually in energy before splitting at approximately 13 nm when reducing donor separations, partially containing an ionic-state nature. The upper (Σ_u^+) branch then crosses the other $1s \rightarrow 3sp$ transitions at a donor separation of approximately 11 nm. The $^1\Pi_g^+$ ($^1\Pi_u^+$) states correspond to the $1s \rightarrow 2p_{xy}$ and $1s \rightarrow 3p_{xy}$ transitions.

The corresponding low-lying triplet excited states with $^3\Sigma_u^+$, $^3\Sigma_g^+$, and $^3\Pi_{u,g}^+$ symmetries are shown (relative to the singlet ground state $^1\Sigma_g^+$) as the dashed curves in Figs. 1(a)–1(c), respectively. There is no charge-transfer state (because of the exclusion principle) and the six transitions converging to $n = 2$ for separated atoms remain almost degenerate down to $d \approx 15$ nm. At this separation, when reducing interdonor distance, one of the $^3\Sigma_u^+$ states rises sharply before becoming the excitation to the $4f\sigma$ orbital in the united atom, while one of the $^3\Sigma_g^+$ states drops sharply to form the $2s\sigma$ excitation in the united atom.

Further insight into the nature of the states can be obtained from their compositions in terms of molecular-orbital excitations. The inset to Fig. 1(a) shows the CI coefficient of the ionic state, arising from the $\sigma_g(1s) \rightarrow \sigma_u^*(1s)$ (bonding to antibonding) transition, in the total wave function of the first $^1\Sigma_u^+$ excited state; the coefficient peaks at a donor distance of ≈7 nm, near the minimum excitation energy. At smaller separations the lowest excitation has only partially ionic character, while at larger separations it remains substantially ionic until the anticrossing at approximately $d = 22$ nm. Similarly, the inset of Fig. 1(d) shows the probability (the square of the CI coefficient) of the doubly excited configuration to the $1s$ antibonding state in the ground-state total wave function; this is a measure of the correlation effects in the ground state that correct the single-particle picture. This probability increases sharply from $\frac{1}{4}$ to $\frac{1}{2}$ at a donor separation of ≈5 nm, corresponding to the evolution from a delocalized molecular-orbital excitation to a localized state with one electron per donor. We can take the separation where the probability reaches $\frac{1}{2}$ (≈10 nm) as an indicator of the location of the Mott transition; this is in reasonable agreement with the experimentally observed transition density [43], as well as with the onset of the broken-symmetry ground state in DFT that will be shown later.

A quantity of particular interest for the optical control of spin couplings, and ultimately for the development of optically controlled quantum gates [21,66], is the triplet-singlet exchange splitting as a function of donor separations. The exchange splitting here is defined as the energy difference between corresponding triplet and singlet states (positive sign means antiferromagnetic, negative sign ferromagnetic). Care must be taken to compare pairs of states that are orbitally similar, and for separations below about 10 nm, intersections among the excited states make it difficult or impossible to define an exchange interaction properly. Figure 1(d) shows the exchange splitting between the $^1\Sigma_g^+$ singlet ground state and the $^3\Sigma_u^+$ triplet ground state. For the exchange splitting in the excited state, supposing we start from a general spin state in the manifold of states dissociating to ground-state atoms; this will be a linear combination of $^1\Sigma_g^+$ and $^3\Sigma_u^+$ ground states. With light polarized along the donor pair axis (z direction), we will excite to a corresponding combination of $^1\Sigma_u^+$ and $^3\Sigma_g^+$, while with light polarized perpendicular to the axis we will make a combination of $^1\Pi_u^+$ and $^3\Pi_g^+$. The exchange splittings between the appropriate $^1\Sigma_u^+$ and $^3\Sigma_g^+$ ($^1\Pi_u^+$ and $^3\Pi_g^+$) states for a single electron excited to $n = 2$ and $n = 3$ shells, are shown in Fig. 1(e) [Fig. 1(f)]. Notice that the splittings are generally antiferromagnetic in sign and, as expected, considerably larger and longer range than the exchange splitting in the ground-state manifold (shown again for comparison). This coupling could be used to realize two-qubit quantum gate operations by using optically excited donor states, as mentioned previously [21].

Figure 2(a) shows the total oscillator strengths of transitions from the overall (singlet) ground state as a function of the interdonor distance and the excitation energy, obtained by using a Lorenz-type broadening with a half-width 0.1 meV (centred at the excitation energies, the height being the oscillator strength) [19]. This shows clearly the positions of optically accessible states for different separations: at large separations, the spectrum is dominated by the $1s \rightarrow 2p$ and $1s \rightarrow 3p$ atomic transitions, while at separations below approximately 20 nm, the charge-transfer band and the corresponding anticrossed (mainly $3sp$) state also contribute strongly to the oscillator strength. The ionic excitation is at ≈17 meV, which is comparable to the experimental results in Ref. [43] if the correction for the lowering of the $1s(A)$ state from the central cell and intervalley effects is included (≈14 meV). The charge-transfer state makes a negligible contribution to the oscillator strength beyond the anticrossing with the $2sp$ excitations ($d >$ 22 nm). In Figs. 2(b) and 2(c), we show the contributions to the oscillator strength along z and x (or y) directions for all the optically accessible states, respectively,

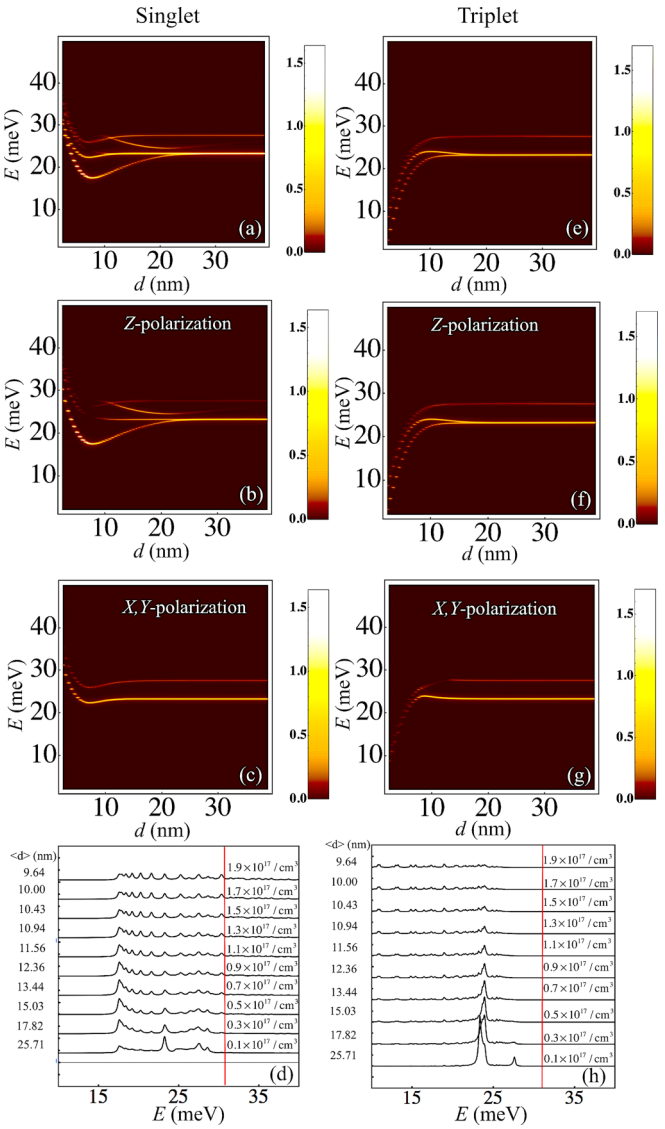

FIG. 2. The optical absorption of DA2 as a function of excitation energy and donor separation. The broadened oscillator strengths for all singlet excitations and all polarizations are shown in (a). The oscillator strengths for polarized excitation along z, and x, y directions are shown in (b) and (c). The corresponding plots for the triplet excitations are shown in (e)–(g). The statistically averaged values of these oscillator strengths for the singlet and triplet sectors, according to the random distribution of the first-nearest neighbors, are shown in (d) and (h), respectively, as a function of excitation energy, for a set of donor densities (0.1×10^{17} to 1.9×10^{17} cm^{-3} with 0.2×10^{17} cm^{-3} increments). We also show the corresponding mean donor distance for each density. The red vertical lines in (d) and (h) correspond to the donor ground-state ionization energy ($\frac{1}{2}$Ha$^* \approx 31$ meV) within the EMT approximation. Only those states converging to $n = 2$ or $n = 3$ transitions at large separations are included.

which correspond to Σ and Π transitions. Figure 2(d) shows the averaged oscillator strength as a function of energy for a distribution of nearest-neighbor distances corresponding to random donor placements with a range of donor densities, where donor pairs are important [22,42,43]. This gives an approximate description of the absorption of a randomly doped crystal under the assumption that pairwise interactions dominate (at least, in the low-energy regime where transitions to other bound states dominate; our basis set is not designed to describe bound-to-continuum transitions at higher energies). For diluted systems the main peak is at the $1s \rightarrow 2sp$ transition energy ($\approx$23 meV), while as the donor density increases (from 0.3×10^{17} to 1.7×10^{17} cm^{-3}), the lower-energy ionic-state excitations strengthen. For each density, we also show the mean donor distance in the continuum limit ($\langle d \rangle = \Gamma(\frac{4}{3})(\frac{4\pi n}{3})^{-\frac{1}{3}}$) on the left-hand side of Figs. 2(d) and 2(h). In Figs. 2(e)–2(h), we show the corresponding plots for triplet excited states as for the singlet sector. Notice that for triplet states the averaged oscillator strengths suggest that the atomic transition is dominant; by contrast, the oscillator strengths of low-energy triplet states at small separations are weak.

2. Three donors

Figures 3(a)–3(d) show the excitation energies of a line of three uniformly distributed donors relative to the ground state ($^2\Sigma_u^+$ symmetry) for low-lying states with $S = \frac{1}{2}$ (doublet) and $S = \frac{3}{2}$ (quartet), as a function of interdonor distance. Low-spin (high-spin) states are plotted by solid (dashed) curves. In total, there are 6 $^2\Sigma_u^+$, 6 $^2\Sigma_g^+$, 3 $^2\Pi_g^+$, and 3 $^2\Pi_u^+$ doublet states, 3 $^4\Sigma_u^+$, 3 $^4\Sigma_g^+$, 2 $^4\Pi_g^+$, and 1 $^4\Pi_u^+$ quartet states, converging to the isolated donor $n = 2$ transitions in the limit of large separations

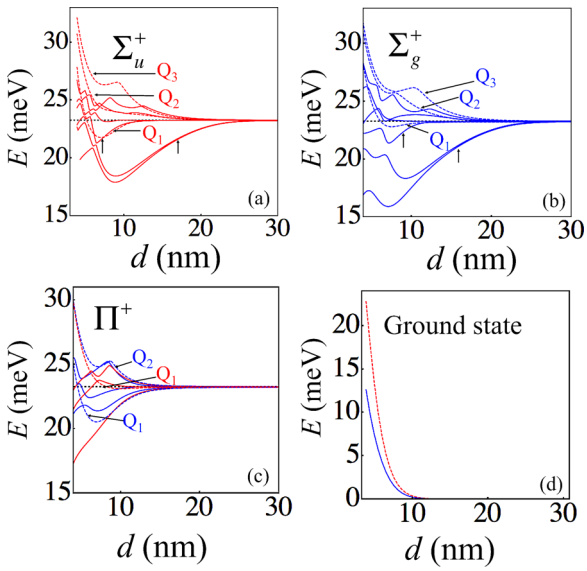

FIG. 3. Excitation energies of DA3 above the ground state as a function of donor separation, computed using FCI methods, are shown. States converging to an excited atom with $n = 2$ are shown for different spatial symmetries: (a) Σ_u^+, (b) Σ_g^+, and (c) $\Pi_{u,g}^+$. Full lines are doublet (low-spin) states, dashed lines (labeled in order to clarify exchange splittings) are quartet (high-spin) states; odd-parity (u) states are shown in red, even-parity (g) in blue. For the Σ symmetries, the vertical arrows point to the ionic states with first nearest-neighbor separation (right vertical arrows) and second nearest-neighbor separation (left vertical arrows). (d) shows the excitation energies of $^4\Sigma_u^+$ and $^2\Sigma_g^+$ states in the lowest manifold of states that dissociate to isolate atoms in the ground state. All the quartet states in (a)–(c) have been labeled for further energy comparison (adopting the same color scheme as others).

as shown in Figs. 3(a)–3(c), and the same numbers converging to $n = 3$ (not shown, for clarity). Note that since the ground state has odd parity, the optically allowed transitions are now to even-parity states (blue curves). In addition, there is a manifold of two low-lying excited states within the $1s$ subspace, one $^2\Sigma_g^+$ and one $^4\Sigma_u^+$, which is the quartet ground state, as shown in Fig. 3(d). At large separations, these two low-lying states converge to spin excited states of the three-spin Heisenberg chain. At smaller separations, they become single-particle excitations into the two excited molecular orbitals formed by linear combinations of the donor $1s$ orbitals.

We now find two different types of ionic states, indicated by the vertical arrows in Figs. 3(a) and 3(b): one branch (right-hand vertical arrow) splits off from the $n = 2$ transitions at approximately $d = 22$ nm as in the two-donor case, and corresponds to an ionic state on first nearest neighbors. The other is at a higher energy (left-hand vertical arrow) anticrossing the $n = 2$ atomic transition at $d \approx 12$ nm, splitting from the $n = 3$ transitions (not shown) at approximately $d = 25$ nm,

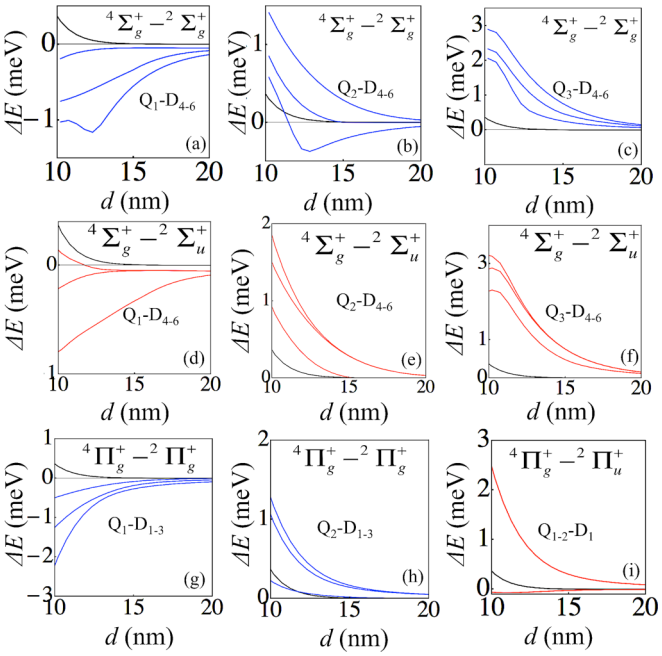

FIG. 4. The exchange splittings between quartet and doublet states in the excited-state manifolds for DA3 as a function of donor spacing: (a)–(c) show splittings between states Q_1–Q_3 respectively of $^4\Sigma_g^+$ symmetry (see Fig. 3) and states D_4–D_6 (excluding the ionic states D_1 to D_3) of $^2\Sigma_g^+$ symmetry (all are excited states converging to $n = 2$ excitations), while (d)–(f) show splittings between corresponding states of $^4\Sigma_g^+$ and $^2\Sigma_u^+$ symmetries. These excitations can all be accessed from the ground-state manifold with polarization along the z direction. Energy differences between even-parity states are in blue, even and odd states in red. (g)–(h) show similar splittings between $^4\Pi_g^+$ and $^2\Pi_g^+$ states (produced by excitations along x and y directions), while (i) shows splittings between $^4\Pi_g^+$ and $^2\Pi_u^+$ states; the color scheme is as for polarization along z direction. The lowest quartet-doublet splitting in the ground-state manifold is also plotted in (a)–(i) for comparison (black curves). Quartet states are ordered from low to high energy as labeled in Fig. 3 (similarly for the doublet states).

and has the electron and hole located on second nearest neighbors. These two types of ionic states anticross each other at $d \approx 5$ nm, where the anticrossing gap of the $^2\Sigma_g^+$ symmetry is much larger than that of the $^2\Sigma_u^+$.

Figure 3(c) shows the low-lying states of Π symmetry (all doubly orbitally degenerate, in the absence of spin-orbit coupling); as for two donors, they all converge to the $n = 2$ energy at large separations, and significant interactions between them on this scale are visible only below separations approximately $d \approx 13$ nm. Figures 4(a)–4(i) show the relevant exchange splittings for excited states that can be accessed by optically allowed transitions from linear combinations of states in the $1s$ low-energy subspace (the $^2\Sigma_u^+$ ground state and the low-lying $^2\Sigma_g^+$ and $^4\Sigma_u^+$ excitations). The relevant excited states therefore include $^2\Sigma_g^+$, $^2\Sigma_u^+$, and $^4\Sigma_g^+$ (for polarization along the z direction), and $^2\Pi_g^+$, $^2\Pi_u^+$, and $^4\Pi_g^+$ (polarization along x or y direction). Figures 4(a)–4(c) [Figs. 4(d)–4(f)] show the splittings between $^2\Sigma_g^+$ ($^2\Sigma_u^+$) states and Q_1-Q_3 of the $^4\Sigma_g^+$ states (see also Fig. 3), respectively. Figures 4(g)–4(h) [Fig. 4(i)] show the corresponding splittings for excitation polarized along x or y direction, between $^2\Pi_g^+$ ($^2\Pi_u^+$) and $^4\Pi_g^+$ states. As in the donor pair (Fig. 1), the exchange splittings are much larger in the excited states than in the-ground state manifold, indicating the potential of optical excitations to control the exchange interaction, and hence implement spin-based quantum gate operations.

In Figs. 5(a)–5(b), we show the broadened oscillator strengths in the three-donor system (DA3) as a function of donor separation and excitation energy, from the doublet ground state $^2\Sigma_u^+$ in (a) and the quartet ground state $^4\Sigma_u^+$ in (b). At a donor separation of ≈7 nm, the ionic states dominate the doublet optical absorption (to a greater extent than for two donors): the lowest charge-transfer transition is the strongest, while the upper one shows signs of anticrossing with the longer-range charge transfer state at approximately $d = 6$ nm. At long range, the intradonor excitation dominates, as in the two-donor case, though the charge-transfer state is more visible than for two donors. The absorption is similar to that of donor pair, the main differences being the splitting of the $n = 2$ excitation at separations around 10 nm and additional low-energy quartet excitations appearing at small separations.

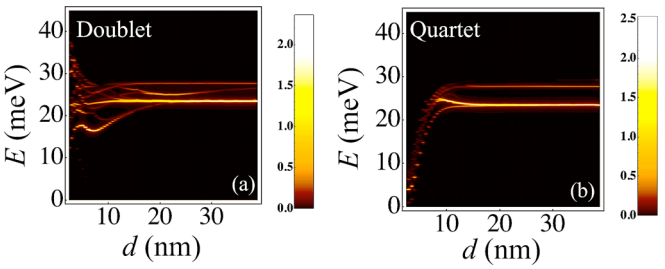

FIG. 5. The broadened oscillator strengths for the doublet and quartet excited states of DA3 are shown in (a) and (b), respectively. For doublet, the ionic states are dominant at the mid-range for donor separation, whereas the atomic transitions are dominant for the long-range. For quartet states, the atomic transitions are clearly important.

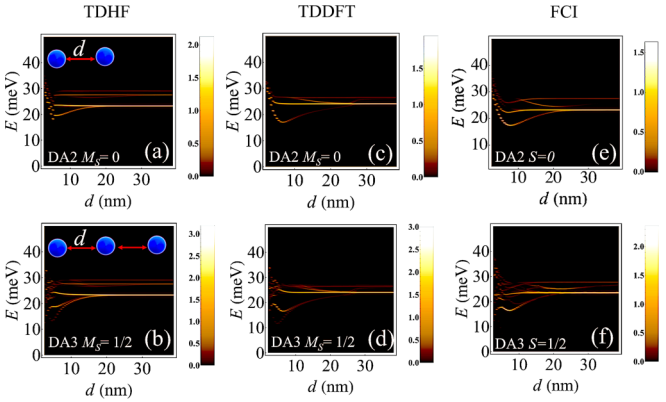

FIG. 6. TDHF [(a) and (b)], TDDFT [(c) and (d)], and FCI [(e) and (f)] calculations for the excited state energies and oscillator strengths of a donor pair and three-donor array, as a function of donor separation, are shown. In the TDHF calculations [(a) and (b)], we can see the ionic excited state, whose energy is higher than that in the TDDFT [(c) and (d)] and FCI [(e) and (f)] calculations when the donor separation is larger than 7 nm. In addition, the transition after the crossover of the $1s \rightarrow 2sp$ is not as clear as the other two calculations. However, TDHF calculations provide a qualitatively similar results to the other two.

B. Longer arrays: TDHF and TDDFT calculations

1. Benchmarking for two and three donors

We first benchmarked the TDHF and TDDFT methods by comparing the results with FCI calculations for a donor pair and three-donor array; excitation energies and oscillator strengths are plotted in Fig. 6, and a quantitative comparison of particular transitions at selected donor separations is shown in Table II. At $d \approx 5$ nm, in the TDHF calculation, there is a jump for the expectation value of $\hat{S}^2$ of the ground state from zero to 0.62, indicating a sudden localization of spin in the broken-symmetry ground state; this leads to an abrupt change of the excitation energies for the ionic states as shown in Fig. 6(a). In contrast, in broken-symmetry TDDFT calculations, $\langle \hat{S}^2 \rangle$ increases to 1 more smoothly.

The TDHF and TDDFT results generally agree qualitatively with the FCI calculations, correctly capturing the substantial contributions from the ionic states and producing the correct long-distance limits (governed by intradonor $n = 2$ and 3 excitations). There are some significant differences in the charge-transfer excitations to ionic states: the excitation energies in TDHF are higher than those in TDDFT or FCI by $\sim$2 meV and cross the $1s \rightarrow 2sp$ excitation at a smaller interdonor separation, and the oscillator strengths beyond this crossover are too weak to see in TDHF as compared with the other two calculations. The other main qualitative discrepancy is the failure of TDHF and TDDFT to capture the minimum in the $n = 2$ excitation [Fig. 2(a)] as a function of separation. Table II shows quantitative comparisons at three different separations: one near the minimum in the charge-transfer band at 7 nm, one in the region dominated by the charge transfer band at 15 nm, and one in the long-distance regime dominated by intradonor excitations at 25 nm. Quantitatively, TDDFT overestimates the oscillator strengths for the $n = 2$ transitions at approximately $d = 7$ nm, but underestimates them at larger separations, whereas TDHF overestimates them for both small and large separations. TDDFT and TDHF also both underestimate the strength of the charge-transfer transition at short range, by up to a factor of two; TDDFT underestimates it throughout, while TDHF calculations overestimate the oscillator strength at longer range.

TABLE II. Comparison of selected results for excitation energy E and oscillator strength f of optical transitions from the low-spin ground state, using FCI, TDHF, and TDDFT approaches for DA2 and DA3 at three different separations. The different transitions are the intradonor $1s \rightarrow 2sp$ transition and the charge-transfer (CT) transition.

			Donor array			
			DA2		DA3	
d (nm)	Transition	method	E (meV)	f	E (meV)	f
7	CT	FCI	17.59	0.44	16.50	0.54
		TDHF	19.66	0.38	16.93	0.15
		TDDFT	17.11	0.21	16.78	0.33
	$1s \rightarrow 2sp$	FCI	24.08	0.00	21.88	0.01
		TDHF	22.94	0.01	23.26	0.00
		TDDFT	23.92	0.04	24.08	0.03
15	CT	FCI	20.86	0.08	21.52	0.03
		TDHF	22.47	0.18	22.30	0.28
		TDDFT	20.99	0.03	21.08	0.03
	$1s \rightarrow 2sp$	FCI	23.20	0.10	23.37	0.12
		TDHF	23.20	0.07	23.26	0.07
		TDDFT	23.98	0.07	24.00	0.08
25	$1s \rightarrow 2sp$	FCI	23.13	0.18	23.38	0.34
		TDHF	23.20	0.26	23.17	0.40
		TDDFT	24.34	0.13	24.24	0.19

2. Four to ten donors

Figures 7 and 8 show the optically accessible excitations based on TDHF and TDDFT for states of uniform DA4–DA10 lines, showing the lowest projections of total spin ($M_S = 0$ for even chains, $M_S = 1/2$ for odd chains). They share a number of qualitative features with one another and with the shorter chains described previously. All have a band of strong absorption at approximately 24 meV (the $n = 2$ intradonor excitation), at an energy that is almost constant down to $d \approx 8$ nm, where it starts to rise sharply. The higher-lying flat bands above approximately 28 meV are the excitations to $n = 3$ and 4 states; for TDDFT, the $n = 3$ states are visibly split by the incompleteness of the basis and (more importantly) by the incomplete cancellation of self-interaction errors. This splitting is not visible for the TDHF calculations. The band of "ionic" states corresponding to excitation across the Mott-Hubbard gap also features prominently in all the chains, as it does in the cases of DA2 and DA3 described previously. In both types of calculations, for separations 7 nm $\leqslant d \leqslant$ 22 nm, the states corresponding to nearest-neighbor charge transfer excitation are approximately degenerate; below 7 nm, they start to become split by hopping interactions between the donors, similar to those that produce splittings between the Σ_u^+ and Σ_g^+ components in the two-donor case [see Fig. 1(a)]. At still smaller separations these excitations transform adiabatically

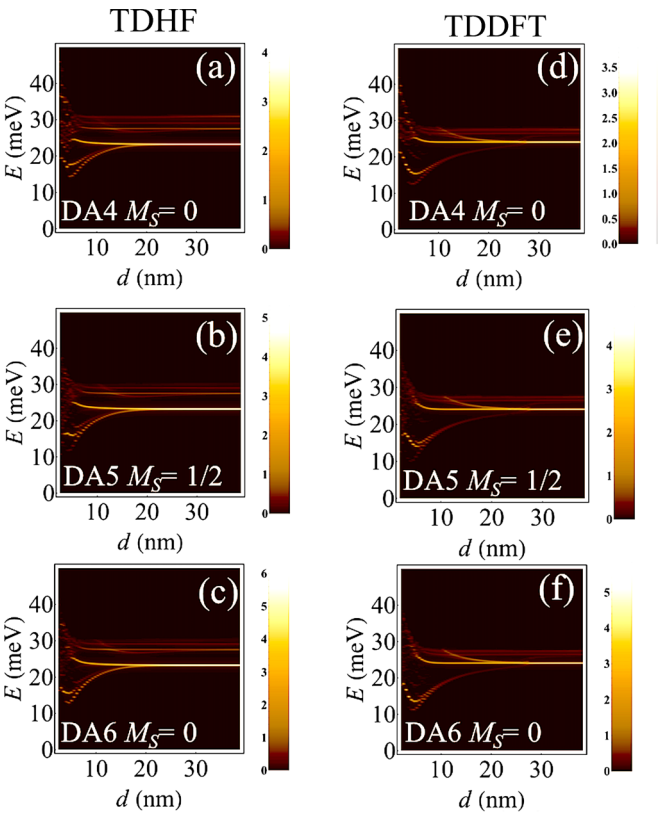

FIG. 7. The broadened oscillator strengths as a function of excitation energy and donor separation for arrays of different sizes from DA4 up to DA6 as calculated in TDHF and TDDFT (in separate columns) are shown in (a)–(f), respectively. Notice that they share generic features: molecular transitions for short separations, charge-transfer bands in the mid-range, and atomic transitions at large separations. The lowest excitation energy falls to ≈10 meV (ionic state, corresponding to a wave length of ≈60 μm) as the number of donors increases.

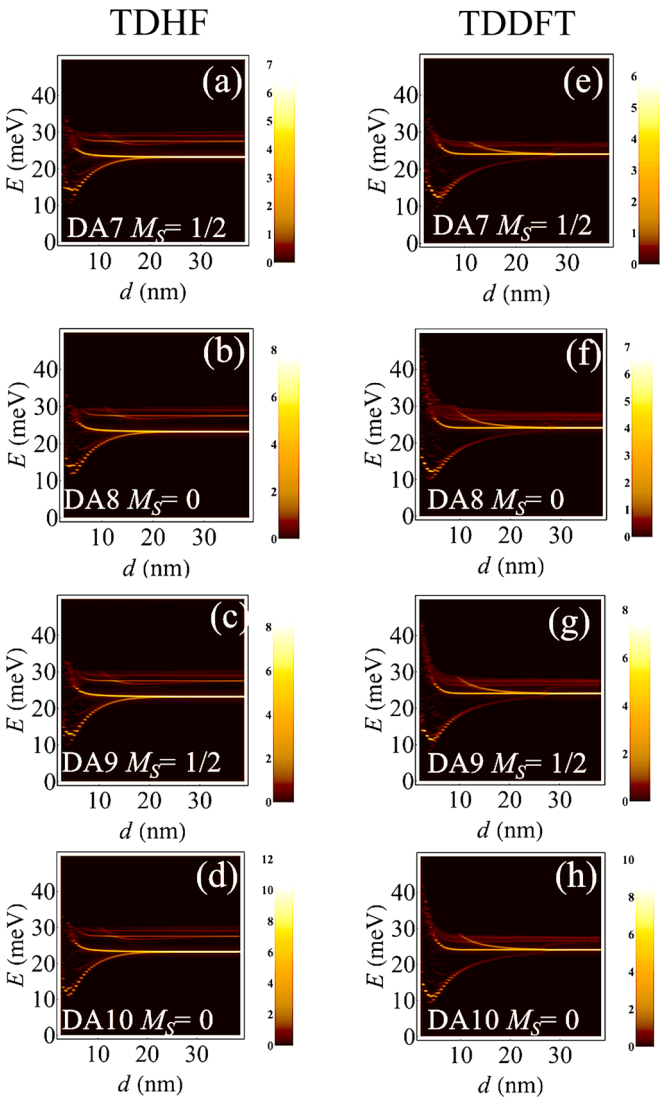

FIG. 8. The broadened oscillator strengths as a function of excitation energy and donor separation for arrays of different sizes from DA7 up to DA10 as calculated in TDHF and TDDFT (in separate columns) are shown in (a)–(h), respectively.

into the single-particle excitations from the 1s bonding state to the corresponding antibonding states; at large separations (above 22 nm) they merge into the $n = 2$ orbital excitation, although the details of the anticrossing observed in the two- and three-donor CI results are not quantitatively reproduced either from TDDFT or TDHF. The minimum excitation energy for TDDFT (TDHF) in this ionic band drops to ≈10(11) meV for long chains. A sequence of further charge-transfer exciton bands with larger electron-hole separations is expected (as suggested by the left arrow in Fig. 3(a) for DA3) but the oscillator strengths for these are exponentially suppressed because of the large charge separations and they are therefore not visible in these plots.

There is also a band of excitations at lower energies, below the Mott-Hubbard gap. At large separations these correspond to the spin excitations of the Heisenberg spin chain; they have very small charge character and correspondingly negligible electric dipole matrix elements with the ground state, and hence would be invisible on the color plots; TDHF and TDDFT do not find them for the lowest spin sectors shown here. As the separation drops (and the ratio t/U in the corresponding effective Hubbard model rises) these excitations acquire an increasing charge character and split as a result of the increasing interdonor hopping. Eventually, the highest-lying members of this manifold are expected to merge with the intersite exciton band at separations where the Mott gap closes. The broken-symmetry ground state come forms above an interdonor distance of ≈10 nm, which is consistent with that predicted by CI calculations.

IV. CONCLUSION

We have computed the excitation energies and optical response for one-dimensional donor arrays in silicon with up to ten dopants within the spherical band approximation. We include a full description of intra and interdonor correlation through our CI calculations on small systems (two- and three-donor arrays), and an approximate description of those correlations through TDDFT calculations for larger systems (from four- up to ten-donor arrays); we also give uncorrelated TDHF results for reference. A comparison with the TDHF

calculations has been made to illustrate the effects of electron correlations; essential features such as ionic excited states are captured by all methods, even though they cannot be well described by single-particle molecular energy levels, but the detailed description within TDHF does not fit the reference CI calculations as well as TDDFT does and in particular the crossing point of the ionic states and the $2sp$ excitation band occurs at at smaller separations in TDHF.

The smallest optically accessible excitation energies within the lowest spin configuration originate from the interdonor ionic charge-transfer state, which becomes dominant at a donor separation of ≈5 to 10 nm, corresponding to a donor density $\approx 3 \times 10^{17}$ to 8×10^{18} cm^{-3}. This donor density region can be well described by a donor-pair model [43]. The donor-separation range where the ionic states are important extends to ≈30 nm (corresponding to a donor density $\approx 3.7 \times 10^{16}$ cm^{-3}). At longer range (>40 nm, corresponding to $< 1.6 \times 10^{16}$ cm^{-3}), intradonor excitations dominate optical transitions. In contrast, at small donor distances (typically smaller than 5 nm), we have a molecular picture for the excitations.

The work presented here treats the molecular-type, charge-transfer, and atomic excited states on the same footing. The first two of these features have been seen in a previous study of the excited states of the one-dimensional Hubbard model [44], where the evolution of the optical spectra was studied and the optical conductivity tuned by varying the ratio of U to t. In the limit of small Mott gaps ($U \ll t$), a holon-antiholon field theory was introduced to describe excitons, whereas for large Mott gaps ($U \gg t$), double occupancy and hole states were used (corresponding to the ionic states found in this paper). By comparing our results for finite arrays obtained in this paper with those from an effective Hubbard model, one could determine the range of donor separations where the effective model is valid, as well as the best-fitting values of the model parameters.

We have also compared the triplet-singlet (and quartet-doublet) energy splittings between a set of appropriate excited states for DA2 (DA3). From our calculations, we can see that the optimal donor distance for optically operating a multiqubit quantum gate is between 10 and 20 nm, where the ground-state exchange is below 0.02 meV but the excited-state exchange is still considerable, as shown in Figs. 1 and 4. A typical excited-state exchange interaction is ≈1 meV at $d \approx 10$ nm, leading to a quantum gate operation time of ≈10 ps, which is much shorter than the typical excited-state relaxation time (≈200 ps) of silicon donors. This result supports the realization of the so-called "control-qubit" scheme [21].

Our results not only address the importance of correlations between donor electrons by using state-of-the-art first-principles tools, but also suggest a trend for the excited states and excitation energies as the number of donors increases, leading to an understanding of the electronic structure of periodic donor arrays. If further combined with CCC and MVE, this type of calculations could provide a more complete picture of the excited states of donor clusters in silicon. These two effects will make the donor orbitals more confined, so we expect the exchange interaction between the ground-state donor and the excited one would be reduced, lowering the optimal distance for quantum computing in the real silicon lattice and also leading to greater sensitivity to donor placement [41]. The donor-array axis direction in silicon is also expected to have a significant effect on exchange interactions (as previously found in the ground-state exchange [41]); this will be investigated in a future publication. TDHF can be useful to include MVE in the donor array calculations. Moreover, these calculations could be useful to assess arrays of impurities in other host materials such as gallium arsenide (GaAs) and germanium, by adjusting the effective-mass parameters.

ACKNOWLEDGMENTS

We wish to acknowledge the support of the UK Engineering and Physical Sciences Research Council Programme under Grant EP/M009564/1. We thank Eran Ginossar, Gabriel Aeppli, Neil Curson, Taylor Stock, Alex Kölker, and Guy Matmon for helpful and inspiring discussions.

[1] F. A. Zwanenburg, A. S. Dzurak, A. Morello, M. Y. Simmons, L. C. L. Hollenberg, G. Klimeck, S. Rogge, S. N. Coppersmith, and M. A. Eriksson, Rev. Mod. Phys. **85**, 961 (2013).

[2] S. R. Schofield, N. J. Curson, M. Y. Simmons, F. J. Ruess, T. Hallam, L. Oberbeck, and R. G. Clark, Phys. Rev. Lett. **91**, 136104 (2003).

[3] M. Usman, J. Bocquel, J. Salfi, B. Voisin, A. Tankasala, R. Rahman, M. Y. Simmons, S. Rogge, and L. C. L. Hollenberg, Nat. Nanotechnol. **11**, 763 (2016).

[4] V. Brázdová, D. R. Bowler, K. Sinthiptharakoon, P. Studer, A. Rahnejat, N. J. Curson, S. R. Schofield, and A. J. Fisher, Phys. Rev. B **95**, 075408 (2017)

[5] B. Weber, S. Mahapatra, H. Ryu, S. Lee, A. Fuhrer, T. C. G. Reusch, D. L. Thompson, W. C. T. Lee, G. Klimeck, L. C. L. Hollenberg, and M. Y. Simmons, Science **335**, 64 (2012).

[6] N. Pascher, S. Hennel, S. Mueller, and A. Fuhrer, New J. Phys. **18**, 083001 (2016).

[7] L. C. L. Hollenberg, A. D. Greentree, A. G. Fowler, and C. J. Wellard, Phys. Rev. B **74**, 045311 (2006).

[8] H. Büch, S. Mahapatra, R. Rahman, A. Morello, and M. Y. Simmons, Nat. Commun. **4**, 2017 (2013).

[9] J. Salfi, J. A. Mol, R. Rahman, G. Klimeck, M. Y. Simmons, L. C. L. Hollenberg, and S. Rogge, Nat. Commu. **7**, 11342 (2016).

[10] M. A. Broome, S. K. Gorman, J. G. Keizer, T. F. Watson, S. J. Hile, W. J. Baker, and M. Y. Simmons, Phys. Rev. B **94**, 054314 (2016).

[11] S. K. Gorman, M. A. Broome, J. G. Keizer, T. F. Watson, S. J. Hile, W. J. Baker, and M. Y. Simmons, New J. Phys. **18**, 053041 (2016).

[12] M. A. Broome, T. F. Watson, D. Keith, S. K. Gorman, M. G. House, J. G. Keizer, S. J. Hile, W. Baker, and M. Y. Simmons, Phys. Rev. Lett. **119**, 046802 (2017).

[13] G. W. Morley, M. Warner, A. M. Stoneham, P. T. Greenland, J. van Tol, C. W. M. Kay, and G. Aeppli, Nat. Mater. **9**, 725 (2010).

[14] A. M. Tyryshkin, S. Tojo, J. J. L. Morton, H. Riemann, N. V. Abrosimov, P. Becker, H.-J. Pohl, T. Schenkel, M. L. W. Thewalt, K. M. Itoh, and S. A. Lyon, Nat. Mater. **11**, 143 (2012).

[15] G. Wolfowicz, A. M. Tyryshkin, R. E. George, H. Riemann, N. V. Abrosimov, P. Becker, H.-J. Pohl, M. L. W. Thewalt, S. A. Lyon, and J. J. L. Morton, Nat. Nanotechnol. **8**, 561 (2013).

[16] P. T. Greenland, S. A. Lynch, A. F. G. van der Meer, B. N. Murdin, C. R. Pidgeon, B. Redlich, N. Q. Vinh, and G. Aeppli, Nature (London) **465**, 1057 (2010).

[17] B. E. Cole, J. B. Williams, B. T. King, M. S. Sherwin, and C. R. Stanley, Nature (London) **410**, 60 (2001).

[18] K. L. Litvinenko, E. T. Bowyer, P. T. Greenland, N. Stavrias, Juerong Li, R. Gwilliam, B. J. Villis, G. Matmon, M. L. Y. Pang, B. Redlich, A. F. G. van der Meer, C. R. Pidgeon, G. Aeppli, and B. N. Murdin, Nat. Commun. **6**, 6549 (2015).

[19] S. Chick, N. Stavrias, K. Saeedi, B. Redlich, P. T. Greenland, G. Matmon, M. Naftaly, C. R. Pidgeon, G. Aeppli, and B. N. Murdin, Nat. Commmun. **8**, 16038 (2017).

[20] K. L. Litvinenko, S. G. Pavlov, H.-W. Hübers, N. V. Abrosimov, C. R. Pidgeon, and B. N. Murdin, Phys. Rev. B **89**, 235204 (2014).

[21] A. M. Stoneham, A. J. Fisher, and P. T. Greenland, J. Phys.: Condensed Matter **15**, L447 (2003).

[22] W. Wu, P. T. Greenland, and A. J. Fisher, arXiv:0711.0084.

[23] T. Hensgens, T. Fujita, L. Janssen, X. Li, C. J. Van Diepen, C. Reichl, W. Wegscheider, S. Das Sarma, and L. M. K. Vandersypen, Nature **548**, 70 (2017).

[24] N. H. Le, A. J. Fisher, and Eran Ginossar, Phys. Rev. B **96**, 245406 (2017).

[25] J. M. Luttinger and W. Kohn, Phys. Rev. **97**, 869 (1955).

[26] W. Kohn and J. M. Luttinger, Phys. Rev. **98**, 915 (1955).

[27] R. A. Faulkner, Phys. Rev. **184**, 713 (1969).

[28] G. Pica, G. Wolfowicz, M. Urdampilleta, M. L. W. Thewalt, H. Riemann, N. V. Abrosimov, P. Becker, H. J. Pohl, J. J. L. Morton, R. N. Bhatt, S. A. Lyon, and B. W. Lovett, Phys. Rev. B **90**, 195204 (2014).

[29] T. H. Ning and C. T. Sah, Phys. Rev. B **4**, 3468 (1971).

[30] K. Shindo and H. Nara, J. Phys. Soc. Jpn. **40**, 1640 (1976).

[31] J. K. Gamble, N. T. Jacobson, E. Nielsen, A. D. Baczewski, J. E. Moussa, I. Montaño, and R. P. Muller, Phys. Rev. B **91**, 235318 (2015).

[32] R. Rahman, C. J. Wellard, F. R. Bradbury, M. Prada, J. H. Cole, G. Klimeck, and L. C. L. Hollenberg, Phys. Rev. Lett. **99**, 036403 (2007).

[33] G. P. Lansbergen, R. Rahman, C. J. Wellard, I. Woo, J. Caro, N. Collaert, S. Biesemans, G. Klimeck, L. C. L. Hollenberg, and S. Rogge, Nat. Phys. **4**, 656 (2008).

[34] Y. L. Hsueh, H. Büch, Y. Tan, Y. Wang, L. C. L. Hollenberg, G. Klimeck, M. Y. Simmons, and R. Rahman, Phys. Rev. Lett. **113**, 246406 (2014).

[35] Y. Wang, C. Chen, G. Klimeck, M. Y. Simmons, and R. Rahman, Sci. Rep. **6**, 31830 (2016).

[36] Y. Wang, A. Tankasala, L. C. L. Hollenberg, G. Klimeck, M. Y. Simmons, and R. Rahman, npj Quantum Information **2**, 16008 (2016).

[37] A. Tankasala, J. Salfi, J. Bocquel, B. Voisin, M. Usman, G. Klimeck, M. Y. Simmons, L. C. L. Hollenberg, S. Rogge, and R. Rahman, arXiv:1703.04175.

[38] A. Dusko, A. L. Saraiva, and B. Koiller, Phys. Rev. B **94**, 115425 (2016).

[39] A. L. Saraiva, A. Baena, M. J. Calderón, and B. Koiller, J. Phys.: Condens. Matter **27**, 154208 (2015).

[40] M. V. Klymenko, S. Rogge, and F. Remacle, Phys. Rev. B **95**, 205301 (2017).

[41] B. Koiller, X. Hu, and S. Das Sarma, Phys. Rev. B **66**, 115201 (2002).

[42] W. Wu and A. J. Fisher, Phys. Rev. B **77**, 045201 (2008).

[43] G. A. Thomas, M. Capizzi, F. DeRosa, R. N. Bhatt, and T. M. Rice, Phys. Rev. B **23**, 5472 (1981).

[44] E. Jeckelmann, F. Gebhard, and F. H. L. Essler, Phys. Rev. Lett. **85**, 3910 (2000).

[45] K. A. Al-Hassanieh, F. A. Reboredo, A. E. Feiguin, I. González, and E. Dagotto, Phys. Rev. Lett. **100**, 166403 (2008).

[46] A. D. Mclachlan and M. A. Ball, Rev. Mod. Phys. **36**, 844 (1964).

[47] R. E. Stratmann, G. E. Scuseria, and M. J. Frisch, J. Chem. Phys. **109**, 8218 (1998).

[48] T. H. Dunning Jr., J. Chem. Phys. **90**, 1007 (1989).

[49] M. J. Frisch *et al.*, *GAUSSIAN 09* (Gaussian, Inc., Pittsburgh, PA, 1998).

[50] H. Nakatsuji and K. Hirao, J. Chern. Phys. **68**, 2053 (1978).

[51] H.-J. Werner, P. J. Knowles, G. Knizia, F. R. Manby, and M. Schütz, WIREs Comput. Mol. Sci. **2**, 242 (2012).

[52] MOLPRO, version 2015.1, a package of *ab initio* programs, H.-J. Werner, P. J. Knowles, G. Knizia *et al.*, see http://www.molpro.net.

[53] P. J. Knowles and N. C. Handy, Chem. Phys. Lett. **111**, 315 (1984).

[54] P. J. Knowles and N. C. Handy, Comp. Phys. Commun. **54**, 75 (1989).

[55] M. Petersilka, U. J. Gossmann, and E. K. U. Gross, Phys. Rev. Lett. **76**, 1212 (1996).

[56] G. Onida, L. Reining, and A. Rubio, Rev. Mod. Phys. **74**, 601 (2002).

[57] E. K. U. Gross, J. F. Dobson, and M. Petersilka, in *Density Functional Theory II: Relativistic and Time Dependent Extensions*, edited by R. F. Nalewajski (Springer, Berlin, Heidelberg, 1996), p. 81.

[58] A. D. Becke, Phys. Rev. A **38**, 3098 (1988).

[59] C. Lee, W. Yang, and R. G. Parr, Phys. Rev. B **37**, 785 (1988).

[60] B. Miehlich, A. Savin, H. Stoll, and H. Preuss, Chem. Phys. Lett. **157**, 200 (1989).

[61] A. D. Becke, J. Chem. Phys. **98**, 5648 (1993).

[62] S. Hirata, M. Head-Gordon, and R. J. Bartlett, J. Chem. Phys. **111**, 10774 (1999).

[63] L. Noodleman, J. Chem. Phys. **74**, 5737 (1980).

[64] T. E. Sharp, Atomic Data **2**, 119 (1971).

[65] W. Kolos and L. Wolniewicz, J. Chem. Phys. **43**, 2429 (1965); **45**, 509 (1966); **48**, 3672 (1968).

[66] V. Filidou, S. Simmons, S. D. Karlen, F. Giustino, H. L. Anderson, and J. J. L. Morton, Nat. Phys. **8**, 596 (2012).